energies

MDPI

Article

Numerical Investigation and Multi-Objective Optimization of Internal EGR and Post-Injection Strategies on the Combustion, Emission and Performance of a Single Cylinder, Heavy-Duty Diesel Engine

Volkan Akgül [1,*], Orkun Özener [1], Cihan Büyük [2] and Muammer Özkan [1]

[1] Internal Combustion Engines Laboratory, Mechanical Engineering Department, Yıldız Technical University, 34349 İstanbul, Turkey; oozener@yildiz.edu.tr (O.Ö.); muaozkan@yildiz.edu.tr (M.Ö.)
[2] TÜMOSAN Engine and Tractor Co., 34010 İstanbul, Turkey; cihan.buyuk@tumosan.com.tr
* Correspondence: volakgul@gmail.com

Abstract: This work presents a numerical study that investigates the optimum post-injection strategy and internal exhaust gas recirculation (iEGR) application with intake valve re-opening (2IVO) aiming to optimize the brake specific nitric oxide (*bs*NO) and brake specific soot (*bs*Soot) trade-off with reasonable brake specific fuel consumption (BSFC) via 1D engine cycle simulation. For model validation, single and post-injection test results obtained from a heavy-duty single cylinder diesel research engine were used. Then, the model was modified for 2IVO application. Following the simulations performed based on Latin hypercube DoE; BSFC, *bs*NO and *bs*Soot response surfaces trained by feedforward neural network were generated as a function of the injection (start of main injection, post-injection quantity, post-injection dwell time) and iEGR (2IVO dwell) parameters. After examining the effect of each parameter on pollutant emission and engine performance, multi-objective pareto optimization was performed to obtain pareto optimum solutions in the BSFC-*bs*NO-*bs*Soot space for 8.47 bar brake mean effective pressure (BMEP) load and 1500 rpm speed condition. The results show that iEGR and post-injection can significantly reduce NO and soot emissions, respectively. The soot oxidation capability of post-injection comes out only if it is not too close to the main injection and its efficiency and effective timing are substantially affected by iEGR rate and main injection timing. It could also be inferred that by the combination of iEGR and post-injection, NO and soot could be reduced simultaneously with a reasonable increase in BSFC if start of main injection is phased properly.

Keywords: internal EGR; post-injection; diesel engine; exhaust emission; engine performance; optimization

Citation: Akgül, V.; Özener, O.; Büyük, C.; Özkan, M. Numerical Investigation and Multi-Objective Optimization of Internal EGR and Post-Injection Strategies on the Combustion, Emission and Performance of a Single Cylinder, Heavy-Duty Diesel Engine. *Energies* **2021**, *14*, 15. https://dx.doi.org/10.3390/en14010015

Received: 11 November 2020
Accepted: 18 December 2020
Published: 22 December 2020

1. Introduction

Due to the strict pollutant emission regulations, diesel engine development studies can be carried out limitedly because of the trade-off relationships between the soot and NO_x emissions which are the inevitable results of the compression-ignition combustion mechanism [1,2]. Although advanced exhaust aftertreatment systems are effective and quite durable, they still impose extra packaging problems and costs for the overall powertrain system. In recent years, studies have been carried out on in-cylinder emission reduction techniques that have the potential to reduce the burden, size and costs of aftertreatment systems [3]. In-cylinder NO_x formation is usually controlled by external exhaust gas recirculation (eEGR), which is a well-known method and is applied by redirecting cooled exhaust gases to the intake manifold [4]. eEGR is effective in lowering the maximum temperature of the burned gases, which is the source of thermal NO_x formation, as it leads to increased thermal capacity, decreased oxygen concentration and dilution of in-cylinder charge [5]. Another way to dilute in-cylinder charge and reduce NO_x emission by lowering

O_2 concentration is to use of internal EGR (iEGR) by controlling in-cylinder residual gases thanks to variable valve actuation (VVA) technology. The application of iEGR with VVA is able to change the charge formation process of the engine very quickly [6] and its reaction to transient operating conditions is much faster, since burnt gases follow a shorter route as compared to eEGR. In addition, the heat losses arising from the use of eEGR are prevented and the in-cylinder charge is heated efficiently with the iEGR. Furthermore, it improves the post cold start capability of the engine by supplying a local feed of chemical species [7].

In this study, the application of iEGR with VVA was carried out by intake valve re-opening during the expansion and exhaust stroke (2IVO), as it provides relatively cooler and higher residual gas fraction than the other strategies such as exhaust valve re-opening (2EVO) [8]. eEGR and iEGR strategies can be carried out without any deterioration in efficiency when certain engine operating parameters such as the combustion phasing are synchronously tuned with EGR [3,9].

However, as is well known, for conventional diesel operation the reduction of the oxygen concentration in the intake air typically increases the engine out soot [3]. High pressure modern common rail injection systems allow multiple injection to improve the combustion and reduce pollutant emissions by precisely controlling the fuel injection process [10,11]. When the main injection timing is adjusted to optimum, split injection has been shown to be a powerful tool that can be used to reduce soot and NO_x emissions in DI and IDI engines simultaneously. It is defined as dividing the main single injection profile in two or more injection pulses with definite delay dwell between the injections [12]. Post-injection, which refers to the small amount of fuel (typically up to approximately 20% of total fuel) [13] injected for a short time after the main injection, is one of the effective multiple injection strategies used to reduce in-cylinder soot emission [14,15].

Balaji et al. [8] conducted experimental and numerical studies to develop an iEGR system on a six cylinder, off-road diesel engine based on modified cam with 2IVO and 2EVO. The results showed that 2IVO has a higher potential of iEGR trapping than 2EVO for the same lift and 2IVO with 1.45 mm secondary lift which yielded 10% iEGR provided 27% reduction in NO_x emission. Millo et al. [16] performed tests with the 2-cylinder IDI diesel engine according to the ECE-40 driving cycle and carried on 1D model simulations for iEGR application through 0.6 mm 2IVO and 1 mm 2EVO strategies. They concluded that 5% and 13% reduction in NO_x emission could be obtained respectively, without causing a significant increase in BSFC and particulate matter (PM) emission. Baratta et al. [5] studied the potential of iEGR and eEGR in reducing the engine-out NO_x emission in a heavy-duty diesel engine at steady-state and transient conditions by means of a refined 1D fluid-dynamic engine model. It has been stated that at steady-state conditions with equal EGR fractions, the NO_x reduction potential of iEGR was lower compared to eEGR and it caused deterioration in BSFC especially in medium-low load. The results in transient conditions showed that iEGR has the potential to control EGR ratio and NO_x emission more accurately, despite little detriment in fuel consumption. Choi et al. [17] investigated the effect of post-injection on the engine-out soot emission for 30% and 60% eEGR conditions. The results concluded that the effect of the post-injection on emissions and combustion is quite different for varying EGR rates. Close post-injection with a dwell of 10 °CA reduced PM emission because of improved fuel distribution for 30% EGR condition and charge cooling effect for 60% EGR. Helmantel and Golovitchev [18] stated that at 10–13 bar indicated mean effective pressure (IMEP) condition with high EGR rate (~41%), additional post-injection to the conventional pilot-main injection scheme significantly reduced soot emission when the post-injection quantity was in the range of 17–30% and the dwell angle was 10–12 °CA away from the start of main injection. While Hotta et al. [19] observed that the combination of close post- injection and high EGR improves the trade-off between soot, fuel consumption and NO_x in a single cylinder, light duty diesel engine; Bobba et al. [20] showed that retarded post-injection timing is much more effective in reducing soot emission. Almeida et al. [21] explored the effect of eEGR and post-injection on combustion characteristics and emissions of a 3.2 L light duty diesel engine. The results implied that post-injection is

effective in reducing the peak heat release of the main injection and EGR usage for the same NO_x level. In addition, it has been stated that post-injection improves soot oxidation by increasing the probability of the fuel finding available oxygen. Cho et al. [22] numerically studied the effect of iEGR application through recompression by reducing exhaust valve lift and duration and post-injection on emission and performance of a 4-cylinder direct injection diesel engine. Their findings showed that the iEGR by recompression is efficient in utilizing heat energy by increasing the EGR rate by about 10%. On the other hand, it was stated that retarded post-injection together with iEGR by VVA improved IMEP, NO_x and indicated specific fuel consumption (ISFC).

To summarize, numerous studies have been carried out showing eEGR, iEGR and post-injection are effectively used to reduce NO_x and soot emissions. However, studies in which EGR and post-injection were applied together were limited with eEGR only and the effect of the EGR and other injection parameters on post-injection efficiency is still unclear. In this respect, the current work is focused on detailed numerical investigation of the post fuel injection and iEGR application with VVA technology for the diesel engine considered and the multi-objective pareto optimization in terms of NO-Soot-BSFC trade-off. For this purpose, 1D engine model created with GT-Power software has been validated with the experimental data at 8.47 bar BMEP and 1500 rpm speed condition and modified for iEGR application with 2IVO. Then, the effect of each parameter on soot, NO and BSFC has been investigated with the help of response surfaces trained by the feedforward neural network. Finally, parameter sets that optimize soot, NO and BSFC have been determined by multi-objective pareto optimization.

2. Methodology

2.1. Engine Modelling

The engine model was created as shown in Figure 1 and validated with the experimental data of the single cylinder diesel engine—the specifications of which are listed in Table 1. The conservation of continuity, energy, and momentum equations (Equations (1)–(3)) [23], which are called Navier–Stokes equations, were solved in one dimension using finite volume scheme. The flow solution was performed by integration of conservation equations in both time and space [24].

$$\frac{dm}{dt} = \sum_{boundaries} \dot{m} \tag{1}$$

$$\frac{d(me)}{dt} = -p\frac{dV}{dt} + \sum_{boundaries} (\dot{m}H) - hA_s\left(T_{fluid} - T_{wall}\right) \tag{2}$$

$$\frac{d(\dot{m})}{dt} = \frac{dpA + \sum_{boundaries}(\dot{m}u) - 4C_f\frac{\rho u|u|dxA}{2D} - K_p\left(\frac{1}{2}\rho u|u|\right)A}{dx} \tag{3}$$

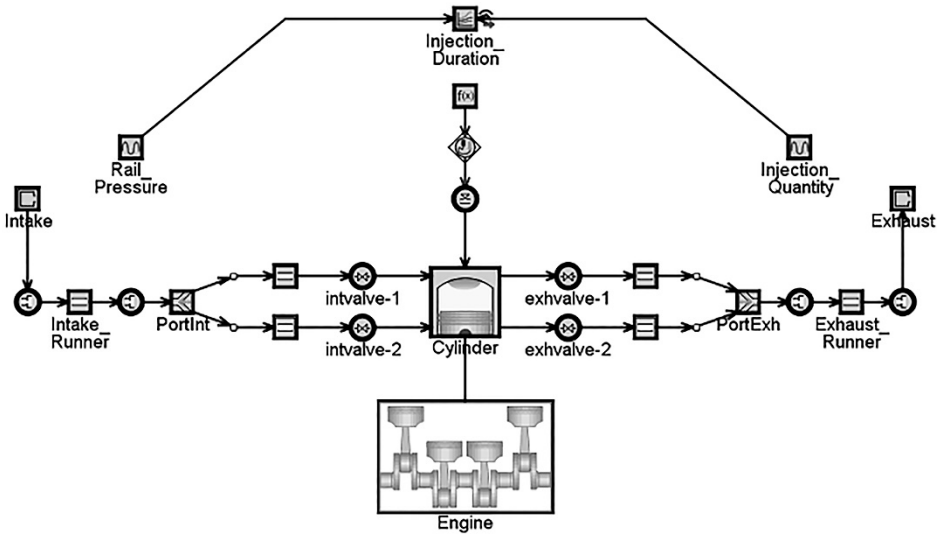

Figure 1. One-dimensional (1D) engine model.

Table 1. Engine and fuel system specifications.

Description	Specification
Engine Type	TÜMOSAN, Single Cylinder, CI
Bore × Stroke [mm]	110 × 120
Total Displacement [l]	1.14
Compression Ratio	15:1
Injection System	Common-Rail
Injector Type	Solenoid actuated
Nozzle Hole Diameter [mm]	0.197
Nozzle Hole Number	8

In the present work, a predictive, phenomenological (based on zone modeling) [25] DIPulse combustion model which can be used for single and multiple injection events in direct injection diesel engines [26] was employed. NO, which is the major component of engine out NO_x, was estimated by three step extended Zeldovich mechanism [27]. The Nagle and Strickland–Constable model [28] has been used to predict the soot emission. In-cylinder heat transfer coefficient was calculated by empirical Hohenberg correlation [29], which is a simplified Woschni correlation [4]. Details of the engine operating condition and injection events for the Baseline (BL) and post injection cases used for the model validation are provided in Table 2.

Table 2. Engine operating conditions for the post injection validation tests.

Parameter		Value					
Speed (rpm)		1500					
Basic Load (bar, BMEP)		8.47					
T_{in} (K)		303					
P_{in} (bar)		2					
P_{rail} (bar)		1000					
m_{total} (mg)		52					
Case No	**BL**	**1**	**2**	**3**	**4**	**5**	**6**
SoI (°CA)	−15	0	−15	−30	0	−15	−30
PFQ (%)	-	10	5	15	15	10	5
α_{post} (°CA)	-	4	20	40	20	40	4

Figure 2 shows the injection rate profile for 52 mg total fuel mass and 1000 bar rail pressure. Here SoI and α_{post} refers to the start of main injection and post injection dwell time between the end of the main injection and the start of the post injection respectively while the PFQ (Post Fuel Quantity) denotes the post injected fuel quantity as a percentage of the total fuel mass injected.

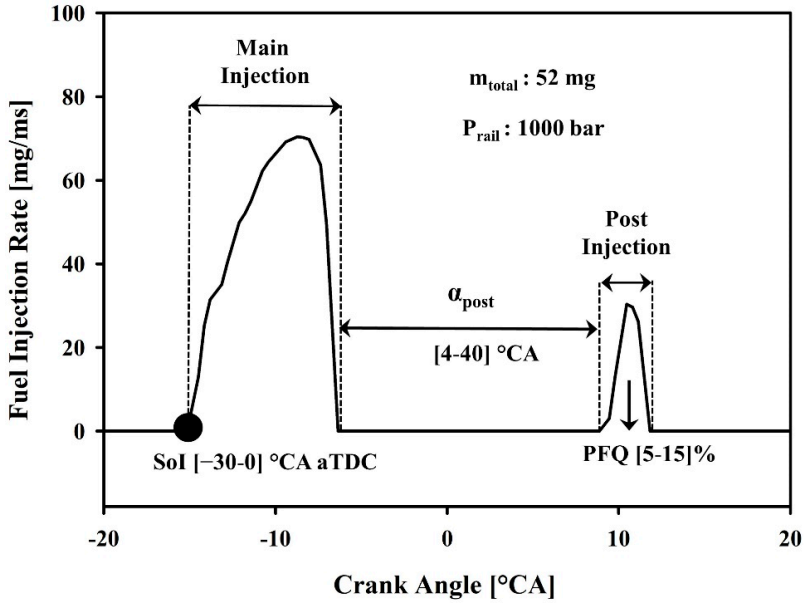

Figure 2. Post injection strategy.

The intake and the exhaust valve lift curves of the test engine are shown in Figure 3. The iEGR application for the engine model was carried out by 2IVO during the expansion and exhaust stroke by returning some of the burned gases in the cylinder to the intake port and releasing it back to the cylinder for the subsequent cycle. The main opening and closing angles of the intake and exhaust valves were kept constant. α_{2IVO} and h_{2IVO} represent the angle between the secondary and the main opening of the intake valve and the maximum valve lift during the 2IVO period, respectively.

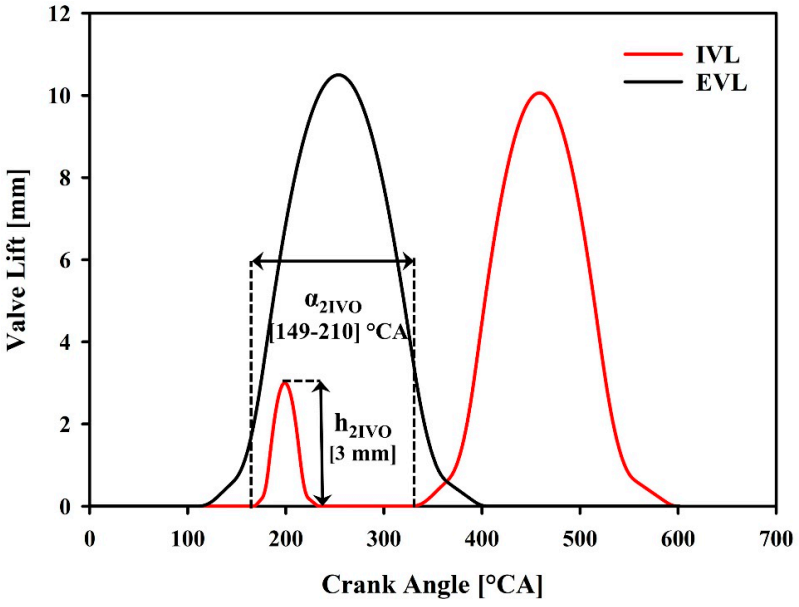

Figure 3. Intake valve lift (IVL), exhaust valve lift (EVL) and 2IVO lift profiles.

Residual gas fraction (RGF) which varies depending on α_{2IVO} for the single injection case is illustrated in Figure 4. For α_{2IVO}: 88 and 118.5 °CA, the RGF is lower than the case when 2IVO is not applied (RGF: 1.28%), since the air flow takes place from the intake port to the cylinder as shown in Figure 5. In the case where α_{2IVO}: 179.5 and 210 °CA, the RGF rises to 16.21% and 28.81% respectively due to growing mass transfer from the cylinder to the intake port. For α_{2IVO}: 149 °CA, mass transfer occurs both from the intake port to the cylinder and vice versa at the time of 2IVO and the RGF is the same as when 2IVO is not employed.

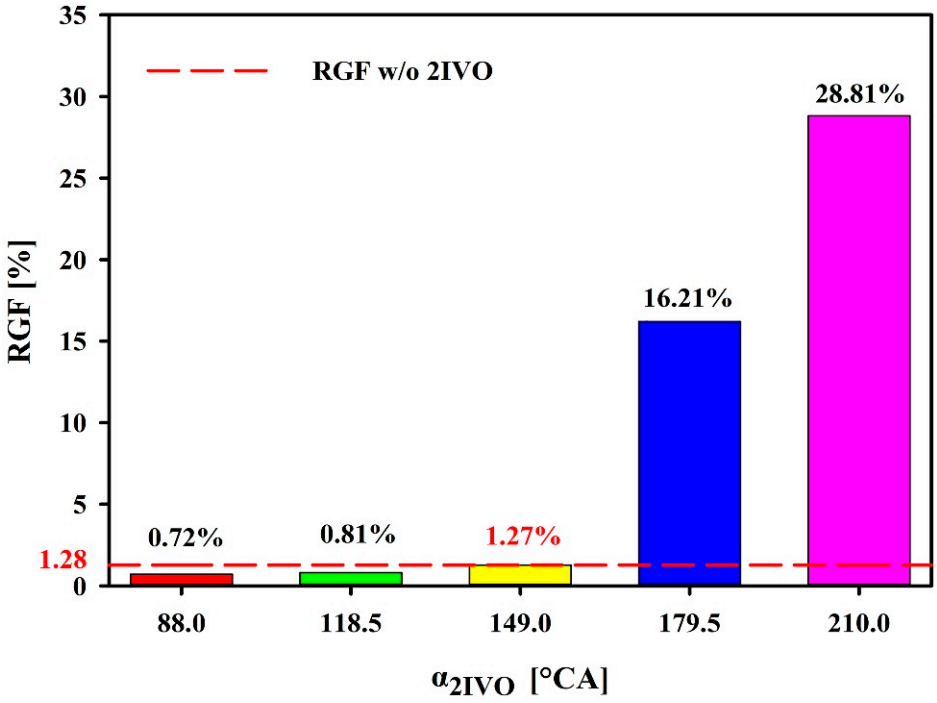

Figure 4. In-cylinder residual gas fraction (RGF) with respect to 2IVO for the single injection case.

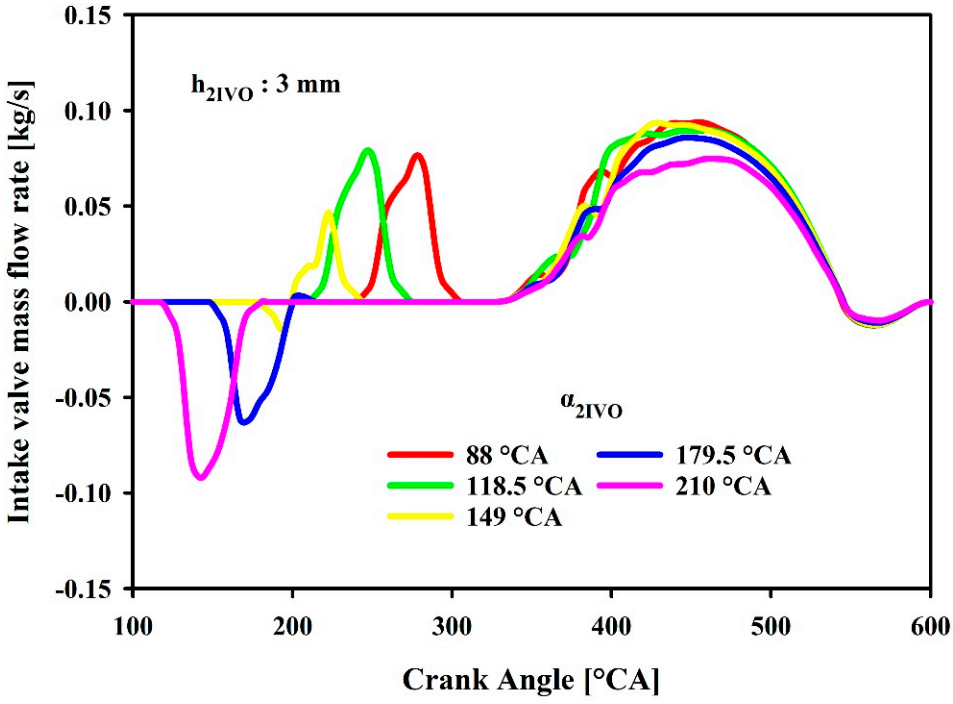

Figure 5. Mass flow rate across the intake valve for varying α_{2IVO}.

2.2. Design of Experiments (DoE) and Multi-Objective Pareto Optimization

Latin Hypercube sampling in which the minimum and maximum values of the parameters and total number of simulation points are defined as in Table 3 was performed in the current study. The maximum values of α_{post} and α_{2IVO} were limited to 40 °CA and 210 °CA, respectively, to prevent the escape of the unburned fuel from the cylinder to the intake port. In addition, α_{2IVO} was determined as 149 °CA for the baseline condition since the in-cylinder conditions such as in-cylinder pressure (ICP) in-cylinder temperature (ICT) and RGF for α_{2IVO}: 149 °CA are exactly the same as the condition when 2IVO is not employed. Based on the design matrix created, a total of 250 simulations were carried out by DIPulse combustion model; the outputs of the analysis points (*bs*Soot, *bs*NO, BSFC and RGF) were fitted by means of a multilayered feedforward neural network and multi-objective pareto optimization [30] with non-dominated sorting genetic algorithm-III (NSGA-III) [31] was employed to obtain parameter sets that minimize *bs*Soot, *bs*NO and BSFC.

Table 3. Latin Hypercube DoE Settings.

Parameter	Unit	Lower Bound	Upper Bound
SoI	°CA aTDC	−30	0
PFQ	%	0	15
α_{post}	°CA	4	40
α_{2IVO}	°CA	149	210
Total number of simulation points: 250			

The multi-objective optimization with n variables, k objectives and m constraints is defined by Equation (4):

$$\min \vec{f}(\vec{x}) \text{ subject to } \vec{x} \in X = \left\{ \vec{x} \middle| \vec{x} \in R^n, g_j(\vec{x}) \leq 0 \ (j = 1, \ldots, m) \right\} \tag{4}$$

$$f_i(\vec{x}) = f_i(x_1, x_2, \ldots, x_n), \ i = 1, \ldots, k \tag{5}$$

$$g_j(\vec{x}) = g_j(x_1, x_2, \ldots, x_n), \ j = 1, \ldots, m \tag{6}$$

where Equation (5) is an objective function vector, and Equation (6) is a constraint condition vector. If there are no other feasible solutions to $\vec{x} \in X$ satisfying:

$$f_i(\vec{x}) \leq f_i(\vec{x}^*), \ ^{\forall} i = \{1, \ldots, k\} \text{ and } f_i(\vec{x}) < f_i(\vec{x}^*), \ ^{\exists} i = \{1, \ldots, k\}, \tag{7}$$

$\vec{x}^* \in X$ is referred to as pareto optimal solution for the specified problem, while a set of pareto optimal solution $f(\vec{x}^*)$ is called pareto front [32,33]. Figure 6 shows the work-flow process from Latin Hypercube design to multi-objective pareto optimization.

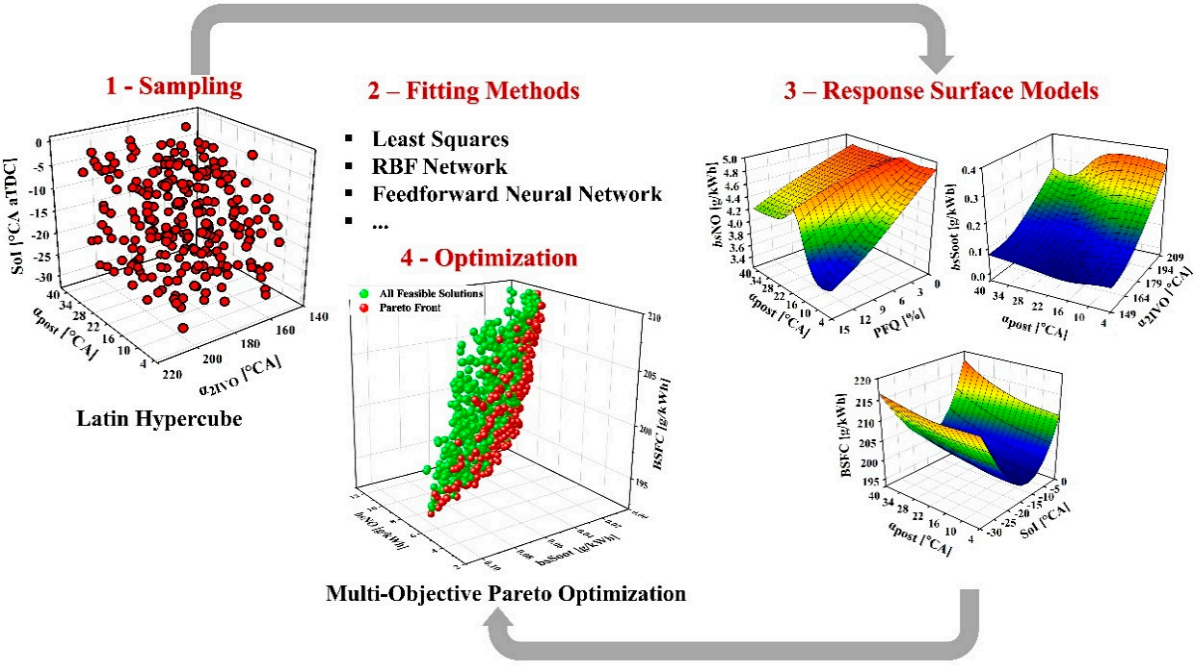

Figure 6. Multi-objective pareto optimization flow chart.

3. Results and Discussion

3.1. Model Validation

As it can be seen from Figure 7, the in-cylinder pressure (ICP), in-cylinder temperature (ICT) and heat release rate (HRR) curves obtained from the model and experimental data showed good agreement, denoting that the numerical model can well represent the combustion process of the engine. The model validation results of the engine tests indicated in Table 2 are shown in Figure 8 in terms of *bs*Soot, *bs*NO and BSFC. It is clearly seen that the results obtained from the model are very close to the experimental data, except for the soot emission due to the inability of the 1D model to adequately capture some of the physical processes in the real engine such as spray formation, turbulence and the 3D structure of the combustion chamber. However, soot trends obtained from the model are similar to the experimental results and acceptable for the purpose of this study.

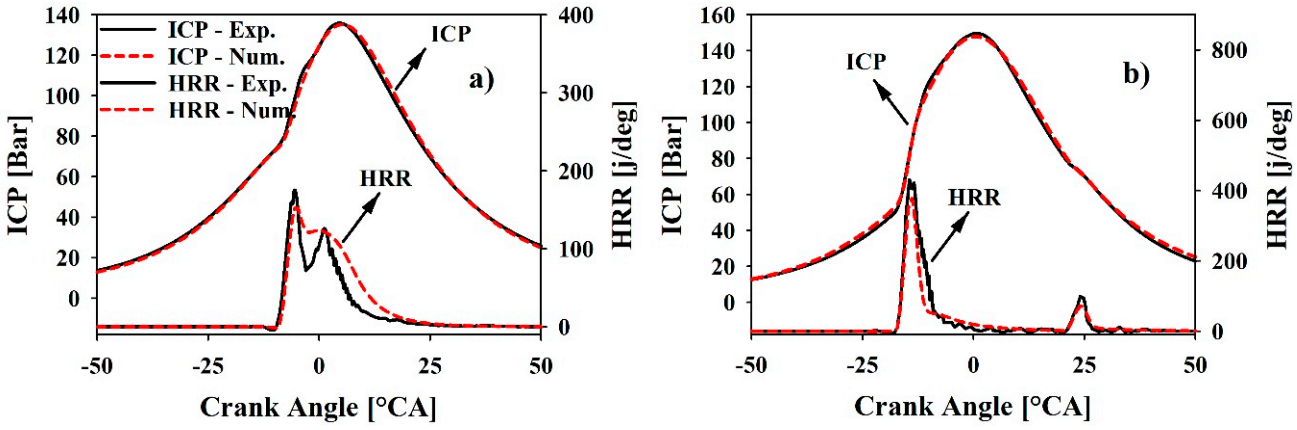

Figure 7. Measured and modelled in-cylinder pressure (ICP) and heat release rate (HRR) for (**a**) the single injection (Baseline) and (**b**) post injection case (Case 3).

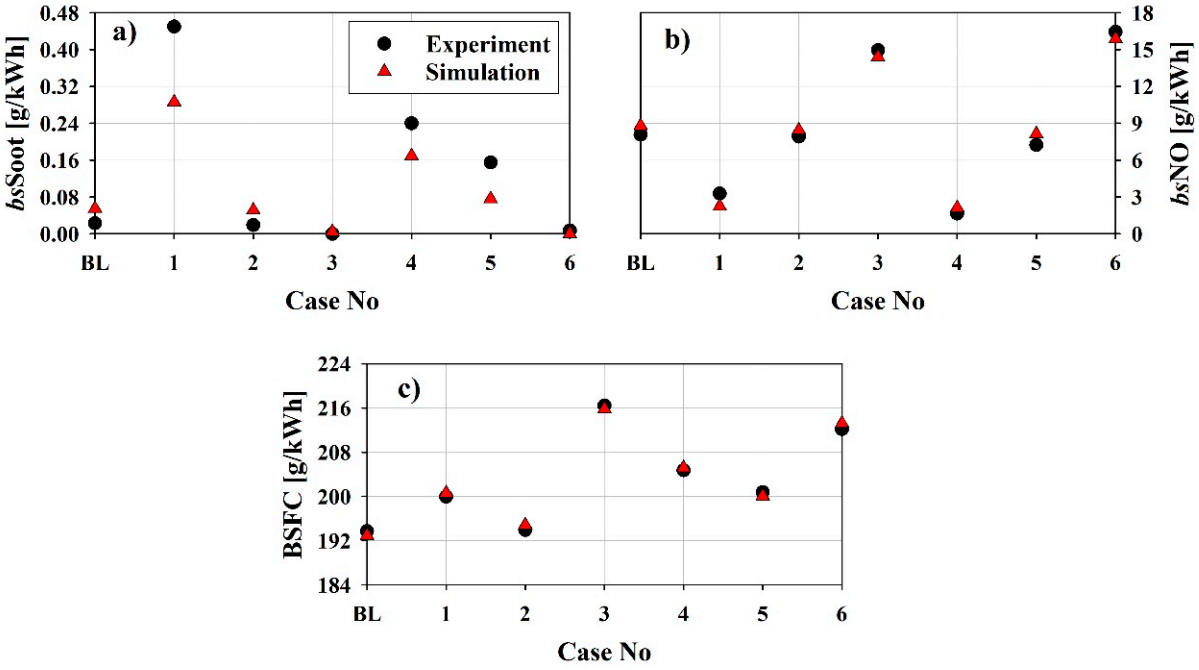

Figure 8. Experimentally measured and model predicted (**a**) *bs*Soot, (**b**) *bs*NO and (**c**) brake specific fuel consumption (BSFC).

3.2. Combustion Analysis

In this section, the effect of iEGR and injection parameters on the in-cylinder combustion characteristics for some selected operating points were examined through the validated 1D model.

Figure 9 illustrates the effect of α_{2IVO} on ICP, ICT and HRR patterns for SoI: −15 °CA, PFQ: 7.5% and α_{post}: 22 °CA. With the addition of residual gases to the intake charge, the first peak of HRR and consequently the maximum ICP decreases as a result of decreasing volumetric efficiency, O_2 concentration and increasing thermal capacity [2]. This effect appears to be higher as α_{2IVO} or iEGR increases [34]. Despite the decrease in O_2 concentration, the ICT shows an increasing trend due to the rise of the high temperature residual gases as α_{2IVO} increases from 149 °CA to 210 °CA [35]. Since the effect of increased ICT and charge dilution at the beginning of the cycle due to iEGR [36] compensated each other, no significant change in ignition delay is observed for the main injection. In the case where α_{2IVO} increases, since the main combustion mostly takes place in the form of diffusion combustion and the main combustion duration is prolonged, post-combustion at α_{post}: 22 °CA occurs while the main combustion proceeds, especially for α_{2IVO}: 210 °CA. Therefore, HRR peak of the post combustion becomes less obvious.

In the case of 7.5% post injection for SoI: −15 °CA and α_{2IVO}: 179.5 °CA, the first peak of HRR for close post injection (α_{post}: 4 and 13 °CA) reduces slightly compared to the single injection due to the reduction in the main injection quantity and keeps constant for the further delayed post-injections (Figure 10). HRR decreases in diffusion combustion phase compared to single injection since the main injection duration is shortened by employing post-injection. Therefore, maximum ICT and maximum ICP decrease slightly [37]. In the case of very close post injection (α_{post}: 4 °CA), despite the slight decrease in maximum ICP compared to the single injection case, the angle at which the ICP is maximum is almost unchanged since the post-combustion still occurs while the main combustion proceeds. As it is clearly understood from the HRR curves in Figure 10, when the post-injection is introduced farther than α_{post}: 4 °CA (e.g., α_{post}: 13, 22, 31, 40 °CA), both the variation in maximum ICP decreases and the angle at which the maximum ICP occurs slightly shifts towards top dead center (TDC) since the post combustion starts to gradually separate from

the main combustion. In addition, as α_{post} gets larger, peak of HRR for the post combustion increases due to reduced equivalence ratio and increased ignition delay [20].

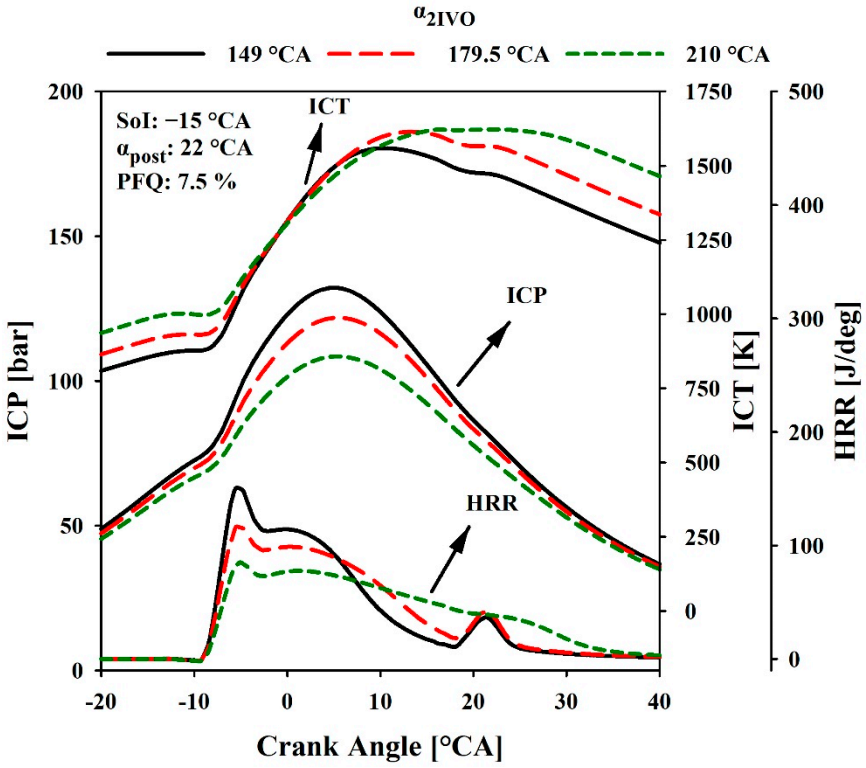

Figure 9. ICP, in-cylinder temperature (ICT) and HRR patterns under different α_{2IVO} conditions.

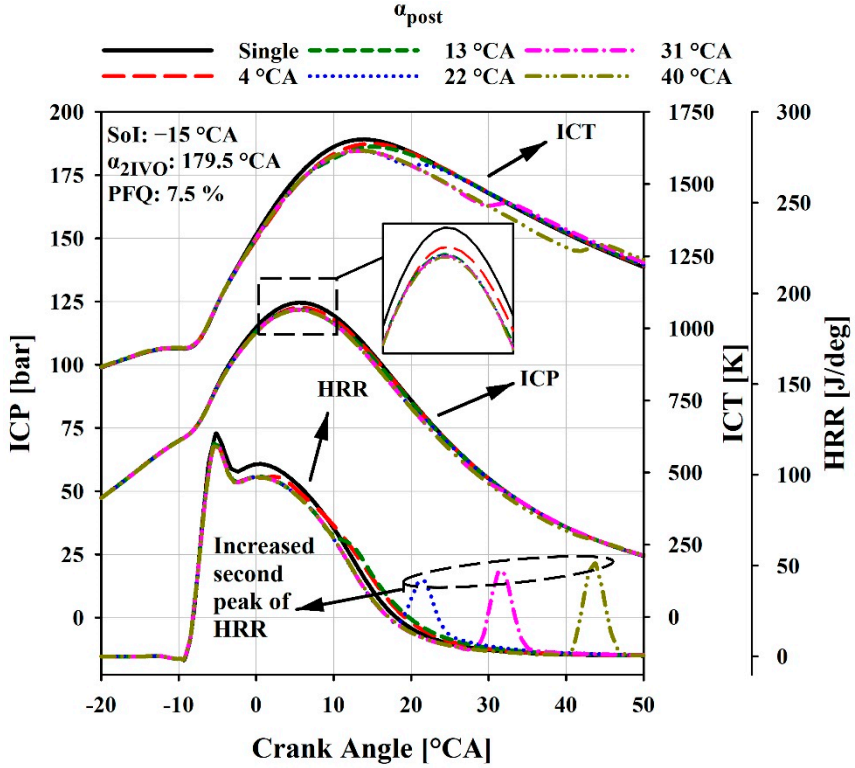

Figure 10. Effect of α_{post} on ICP, ICT and HRR pattern.

ICP, ICT and HRR patterns for SoI: −15 °CA, α_{2IVO}: 179.5 °CA and α_{post}: 22 °CA are delineated in Figure 11 for 5%, 10% and 15% PFQ. It is clearly seen from the figure that as PFQ increases, the second peak of HRR rises [38] and the first peak of HRR reduces slightly as mentioned before. In addition, as PFQ increases, the amount of fuel in the main jet and therefore HRR decreases in diffusion-controlled combustion phase [39]. Thus, maximum ICT and maximum ICP reduce accordingly.

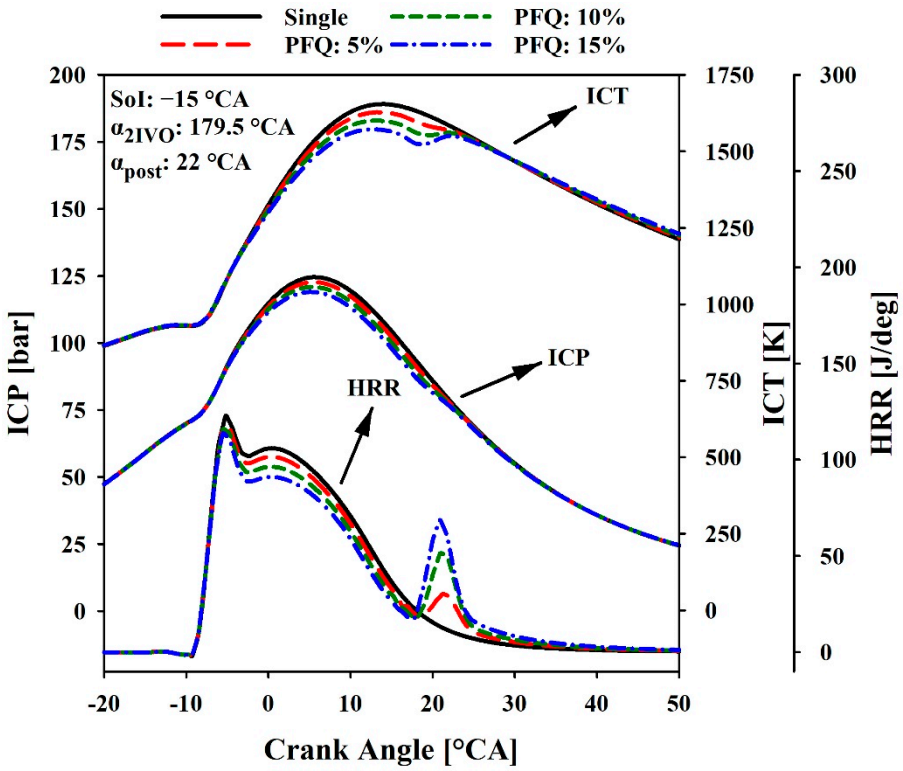

Figure 11. Effect of PFQ on ICP, ICT and HRR pattern.

Figure 12 depicts the ICP, ICT and HRR for varying SoI timings in the case where α_{2IVO}: 179.5 °CA, PFQ: 7.5%, and α_{post}: 22 °CA. Because of the relatively high ICT at the start of the main injection for SoI: 0 °CA and the associated short ignition delay [40], the HRR peak for the premixed combustion is not apparent and the combustion caused by the main injection takes place almost completely in the form of diffusion combustion. Since the combustion occurs at a point far from TDC in the expansion stroke, the ICP at the moment of combustion is lower than the ICP at the end of the compression stroke. With the advance of SoI to −15 °CA, ignition delay increases due to the relatively low ICT at the start of main injection, and thus, the premixed combustion HRR peak begins to appear [41]. In addition, maximum ICP and maximum ICT increase since the main combustion takes place closer to TDC. Advancing SoI further to −30 °CA causes a significant rise in the first peak of HRR due to a longer ignition delay, which tends to promote more premixed combustion and increase in maximum ICT and maximum ICP [42–44]. Furthermore, it can be clearly seen from the figure that as SoI is advanced from 0° CA to −30 °CA, ignition delay for post injection and therefore second peak of HRR decrease since α_{post} is constant and post injection is performed at higher ICT conditions.

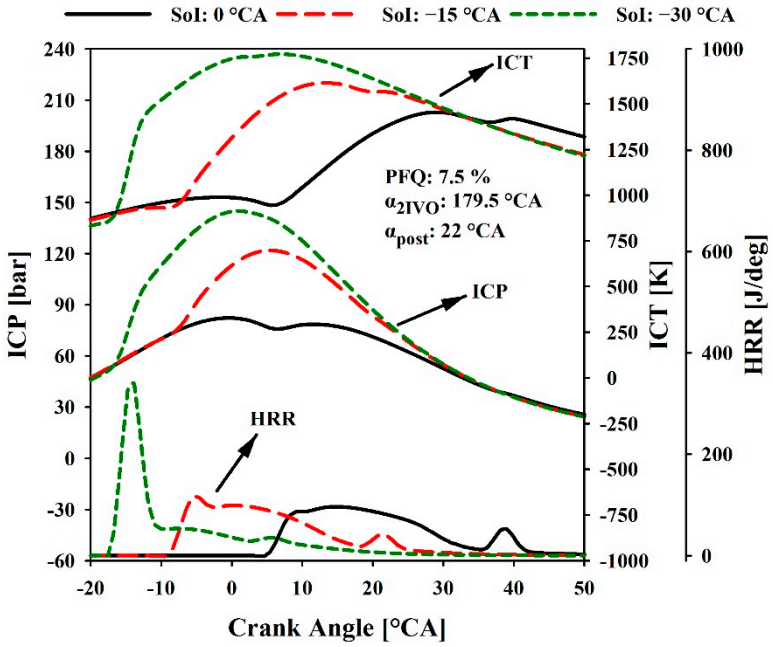

Figure 12. ICP, ICT and HRR patterns for various SoI timings.

3.3. Emission and Performance Analysis

In the following section, effect of iEGR with 2IVO and post injection parameters on the formation and oxidation mechanisms of NO and soot emissions and BSFC were discussed with some of the selected trained response surfaces. While examining the effect of any two parameters on the specified output, other parameters were kept constant at their average values of the design intervals indicated in Table 3.

Figure 13a shows the variation in *bs*Soot with respect to α_{post} for varying SoI timings. Considering the soot emissions for SoI: 0 °CA, it is seen that the soot emission is higher in the case of very close post injection (e.g., α_{post}: 4, 8 and 12 °CA) due to the penetration of the post-injected fuel into the zone with higher equivalence ratio and higher temperature resulting from the main combustion (Figure 10) [45].

When the post injection is delayed to some extent (e.g., α_{post}: ~22 °CA), soot emission decreases and reaches the minimum level due to reduced local equivalence ratio [45] and sufficient temperatures still available for soot oxidation. With further delay of α_{post} up to 40°CA, soot oxidation deteriorates due to the lower ICT at the time of post injection and soot emission starts to increase. As a result of advancing the SoI from 0 °CA to −30 °CA, maximum ICT increases (Figure 12), and the soot emission decreases due to enhanced soot oxidation [46]. As indicated in Figure 13b, the reduced O_2 concentration due to increased α_{2IVO} causes higher soot emission because of the fuel rich zones [4,47]. With the increase of α_{2IVO}, the α_{post} angles at which soot oxidation is maximum is delayed. This can be attributed to temperatures which may enable maximum soot oxidation can be obtained for larger α_{post} due to rising ICT (Figure 9) resulting from the increased α_{2IVO} and relatively lower local equivalence ratio at the time of delayed post injection. As clearly seen in the Figure 13c, as PFQ increases, the soot emission increases in the case of close post injection where the soot formation is maximum (e.g., α_{post}: 4, 10 °CA) and decreases in the case of relatively late post injection where the soot oxidation is maximum (e.g., α_{post}: ~26 °CA).

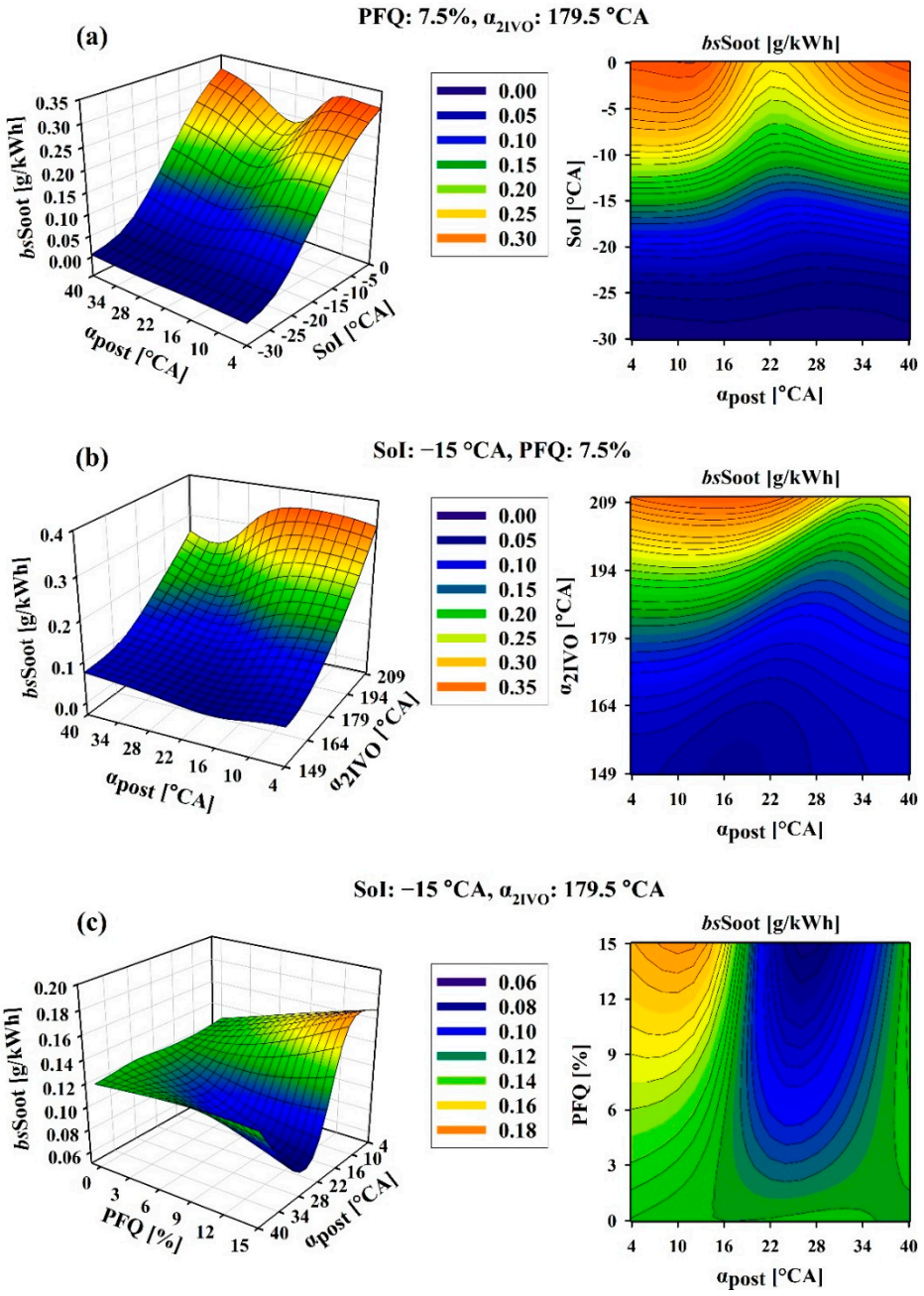

Figure 13. *bs*Soot response surfaces for (**a**) α_{post}—SoI, (**b**) α_{post}—α_{2IVO} and (**c**) PFQ—α_{post}.

Figure 14a illustrates the variation in *bs*NO with respect to α_{post} for varying SoI timings. It is obvious from the figure that *bs*NO increases as SoI is advanced [44] due to the increasing ICT (Figure 12). In the case of post injection up to α_{post}:~18 °CA for SoI: 0 °CA, *bs*NO slightly increases as compared to close post injections partially due to the extended duration of the NO formation caused by the main combustion and partially to the improved post combustion (Figure 10) due to the decreased equivalence ratio. It should also be noted that the α_{post} angle at which the *bs*NO starts to increase slightly is also delayed as SoI is advanced. *bs*NO decreases as α_{2IVO} increases as shown in Figure 14b, and the α_{post} angles where NO emission starts to increase slightly also delays as α_{2IVO} gets larger since the local equivalence ratio that will allow NO formation can be obtained in larger α_{post} as RGF incre-ases. From the Figure 14c, it can be concluded that the increasing PFQ reduces *bs*NO compared to single injection (PFQ: 0%) due to the increasing O_2 consumption of the post combustion and decreasing ICT resulting from the reduced

main injection quantity (Figure 11) [48] in the case of close post injection (e.g., α_{post}: 4 and 10 °CA) and only due to the reduction in the main injection quantity in the case of retarded post injections (e.g., α_{post}: 28, 34 and 40 °CA).

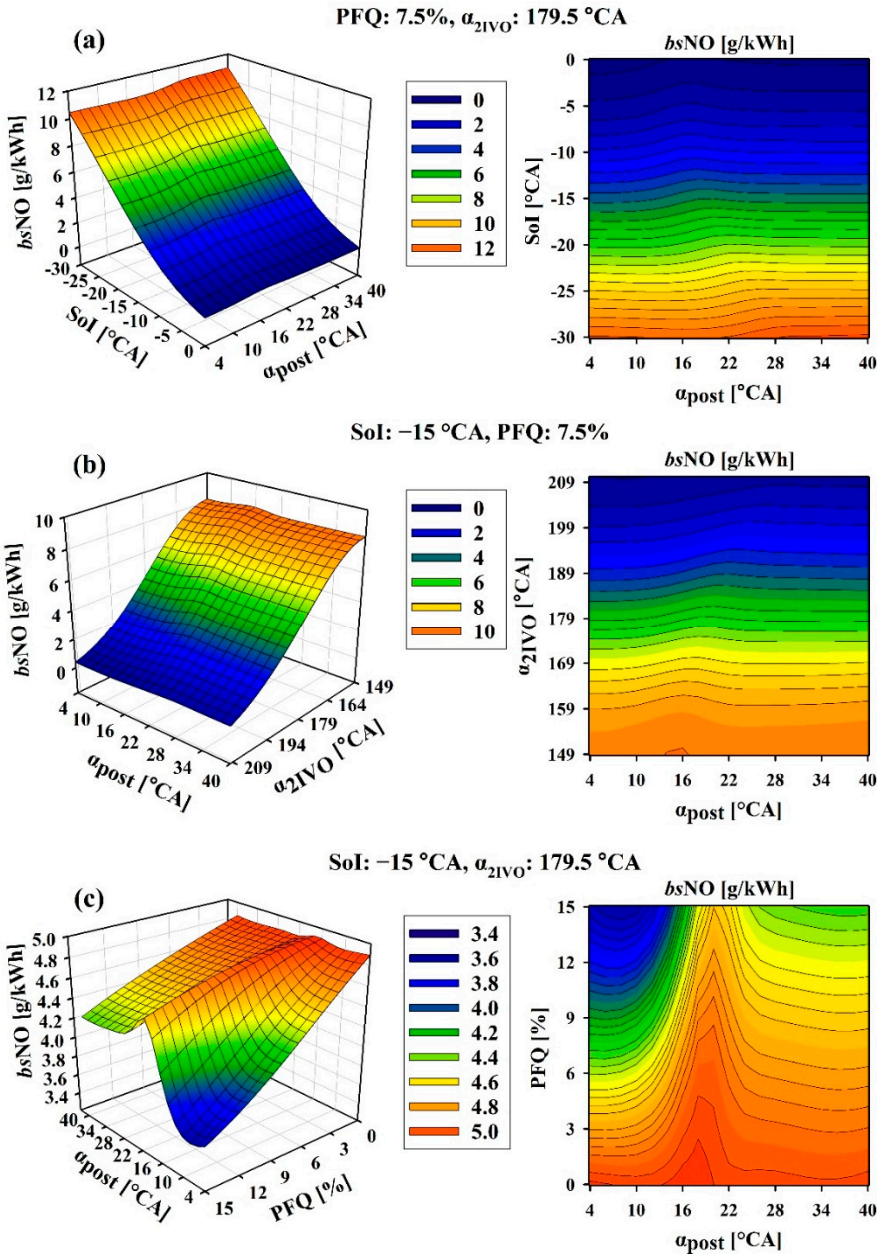

Figure 14. *bs*NO response surfaces for (**a**) α_{post}—SoI, (**b**) α_{post}—α_{2IVO} and (**c**) PFQ—α_{post}.

As shown in Figure 15a, BSFC is minimum for SoI: −12 °CA and α_{post}: 4 °CA. When SoI is delayed to 0 °CA, BSFC increases compared to SoI: −12 °CA as the start of combustion shifts towards the expansion stroke (Figure 12) and the contribution to power production decreases due to the reduction in maximum ICP [44]. On the other hand, by advancing SoI to −30 °CA, maximum ICP increases but the crank angle at which the ICP is maximum become closer to TDC, and more significant part of the pressure rise occurs before the TDC (Figure 12) leading to rise in BSFC [42]. As the α_{post} increases for SoI: 0 °CA, BSFC increases due to the reduction in the contribution of post injection on power production [49]. Despite that, BSFC slightly improves up to α_{post}: ~15 °CA for SoI: 30 °CA as the amount of fuel burned in the compression stroke reduces. As it can be inferred from the Figure 15b, increasing α_{2IVO} and therefore RGF deteriorates BSFC due to the reduced volumetric

efficiency and O_2 concentration [2]. In addition, the rate of increase in BSFC due to α_{post} decreases slightly for the greater α_{2IVO} angles. Lastly, Figure 15c shows that the increase in BSFC due to rising PFQ is much more pronounced as α_{post} increases due to the decreasing contribution of the post injection on power production.

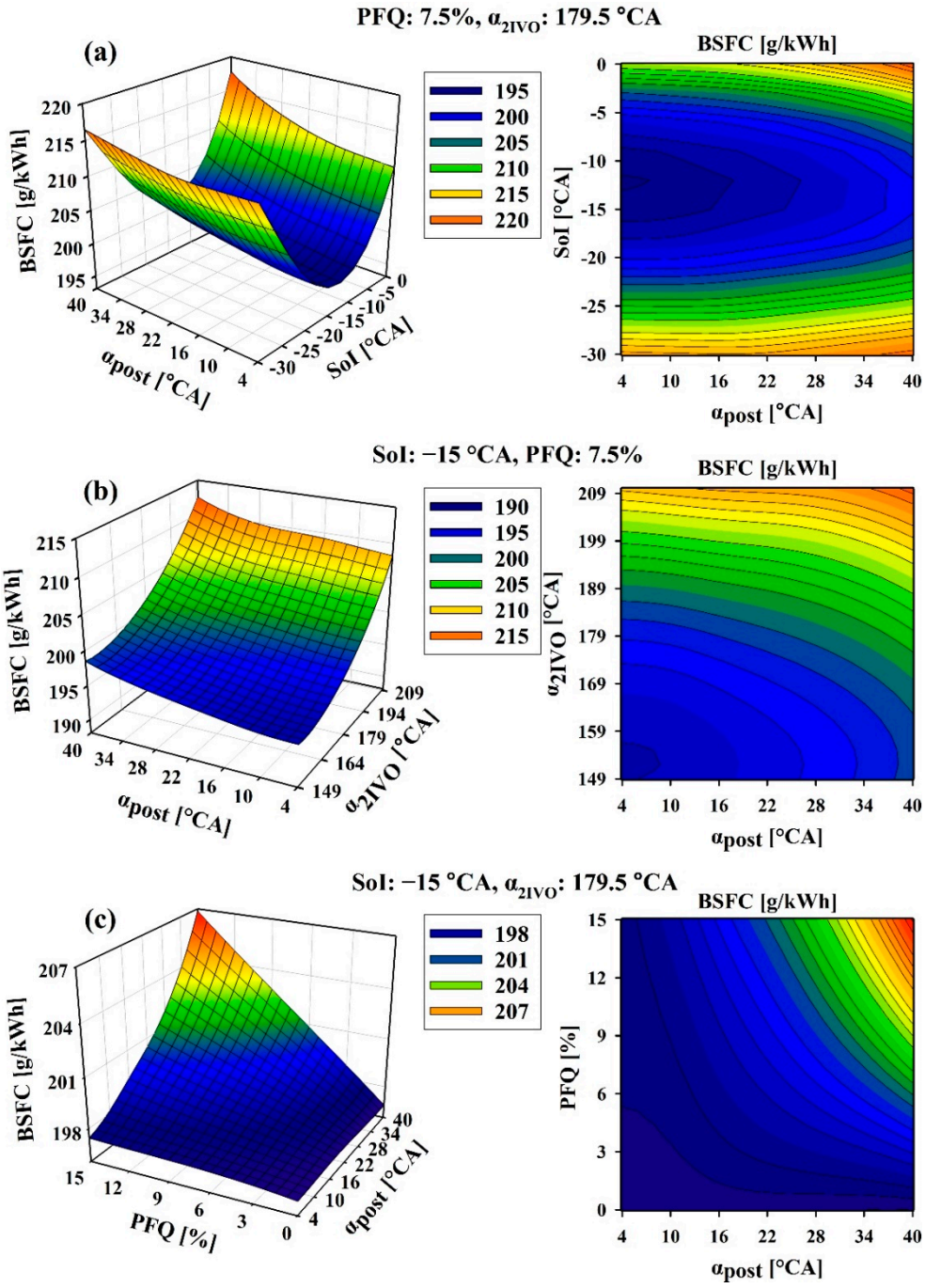

Figure 15. BSFC response surfaces for (**a**) α_{post}—SoI, (**b**) α_{post}—α_{2IVO} and (**c**) PFQ—α_{post}.

3.4. Multi-Objective Optimization

During the optimization process, six constraints were applied to eliminate negative results and prevent excessive increase in BSFC, *bs*NO and *bs*Soot [50]. Consequently, the design space was limited to 0.1 g/kWh, 12 g/kWh and 210 g/kWh in terms of *bs*Soot, *bs*NO and BSFC, respectively. Figure 16 shows all feasible solutions (green points) and pareto optimum solutions (red points) generated by the NSGA-III algorithm within the specified constraints. Because the optimization contained three unique objectives, the pareto front

contains the sets of four engine design variables which minimizes these three objectives differently [51]. The generated pareto front which consists of design points with varying *bs*NO, *bs*Soot and BSFC is shown in Figure 17.

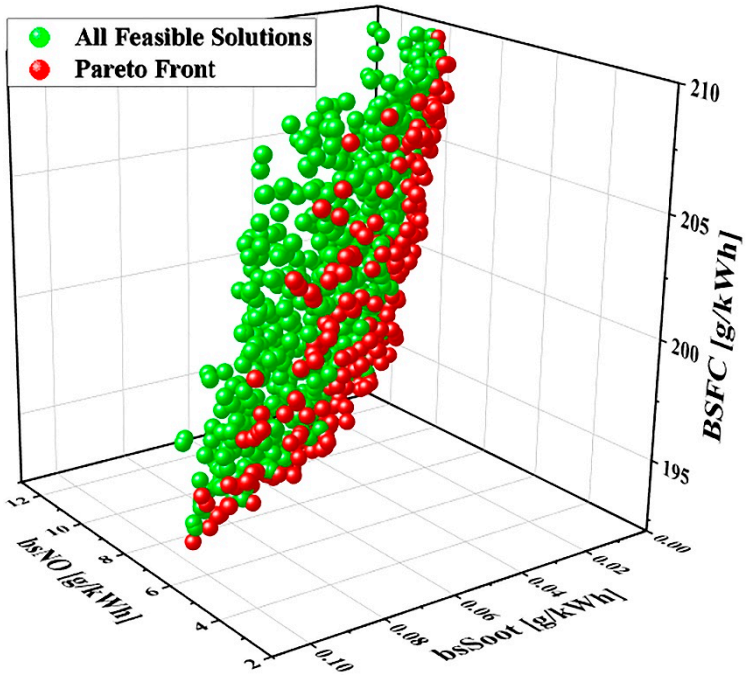

Figure 16. All feasible solutions and pareto frontier in the *bs*NO—*bs*Soot—BSFC objective space.

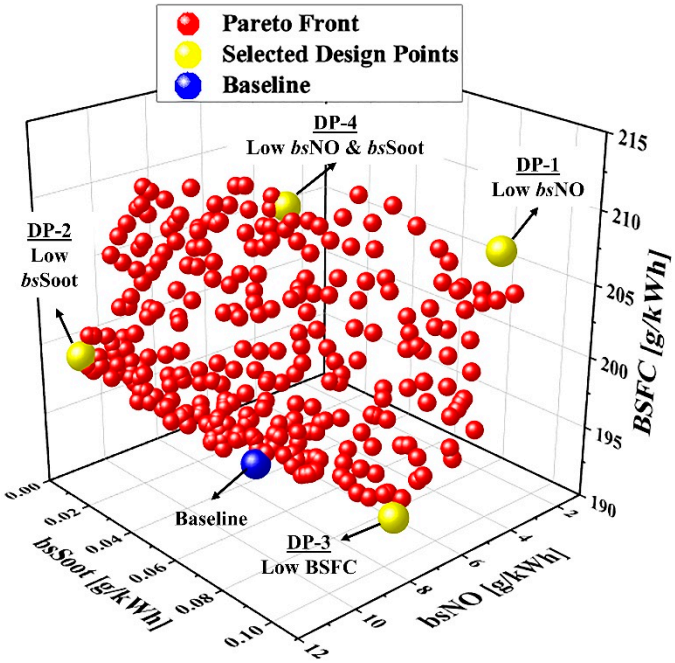

Figure 17. *bs*NO—*bs*Soot—BSFC pareto front and selected optimum design points.

Table 4 shows the input parameter values for the four optimum design points (DPs) selected from the entire pareto front, the objective values obtained from the response surface models (RSM) and confirmation simulations carried out by the 1D model, the deviation of the RSM results with respect to 1D model and the variation of the objective values of the optimum design points with respect to the Baseline case based on the 1D model

results. The baseline (BL) represents the single injection case (SoI: −15 °CA aTDC) without iEGR and the evaluations were carried out by comparing the BL case with the selected design points. The RGF output specified in the table was not defined as an objective in the optimization process and was included only to observe their values in optimum design points.

Table 4. Design variables and objective values corresponding to selected four optimal design points.

DPs	Design Variables					Objectives			
-	SoI (CA aTDC)	PFQ (%)	α_{post} (°CA)	α_{2IVO} (°CA)		*bs*Soot (g/kWh)	*bs*NO (g/kWh)	BSFC (g/kWh)	RGF (%)
BL	−15	0	0	149	RSM	0.0498	8.8109	193.5786	1.2278
					1D Model	0.0549	8.7983	193.7229	1.2709
					Error (%)	−9.29	+0.14	−0.07	−3.39
					Variation (%)	-	-	-	
DP-1	−18.29	12.57	32.15	195.97	RSM	0.0952	2.888	207.2265	24.1377
					1D Model	0.0919	2.9217	207.1815	24.1287
					Error (%)	+3.59	−1.15	+0.02	+0.04
					Variation (%)	▲67.4	▼66.79	▲6.95	
DP-2	−20.70	2.60	16.24	155.11	RSM	0.0109	11.3309	199.6339	2.2404
					1D Model	0.0099	11.3523	199.4705	2.2292
					Error (%)	+10.1	−0.19	+0.08	+0.5
					Variation (%)	▼81.97	▲29.03	▲2.97	
DP-3	−11.99	0.65	11.5	150.12	RSM	0.0952	7.2344	192.3003	1.387
					1D Model	0.0965	7.2478	192.4023	1.3725
					Error (%)	−1.35	−0.18	−0.05	+1.06
					Variation (%)	▲75.77	▼17.62	▼0.68	
DP-4	−22.92	10.47	33.84	188.66	RSM	0.0407	5.9497	208.4513	20.9319
					1D Model	0.0381	5.9689	208.4541	20.9297
					Error (%)	+6.82	−0.32	−0.001	+0.01
					Variation (%)	▼30.6	▼32.16	▲7.6	

Figure 18 shows the ICP, ICT and HRR traces for the baseline case and selected design points. Although the SoI was slightly advanced (−18.29 °CA) at DP-1, which expresses the "low *bs*NO" condition, by re-opening the intake valve at α_{2IVO}: 195.97 °CA (RGF: 24.1287%) and introducing 12.57% post injection at α_{post}: 32.15 °CA, the first peak of HRR and maximum ICP decreased with respect to baseline case. In contrast, the ICT at the beginning of the cycle and maximum ICT increased by the hot residual gases. The lower ICP compared to baseline condition at the beginning of the cycle is due to the decrease in volumetric efficiency caused by the iEGR. By advancing the SoI and employing post injection, higher soot emission due to iEGR could be kept below the limit of 0.1 g/kWh. As a result of iEGR application, post injection and the slight advance of SoI, NO emission decreased by 66.79%, from 8.8109 to 2.9217 g/kWh, soot emission increased by 67.4% from 0.0549 to 0.0919 g/kWh and BSFC increased by 6.95% from 193.7229 to 207.1815 g/kWh.

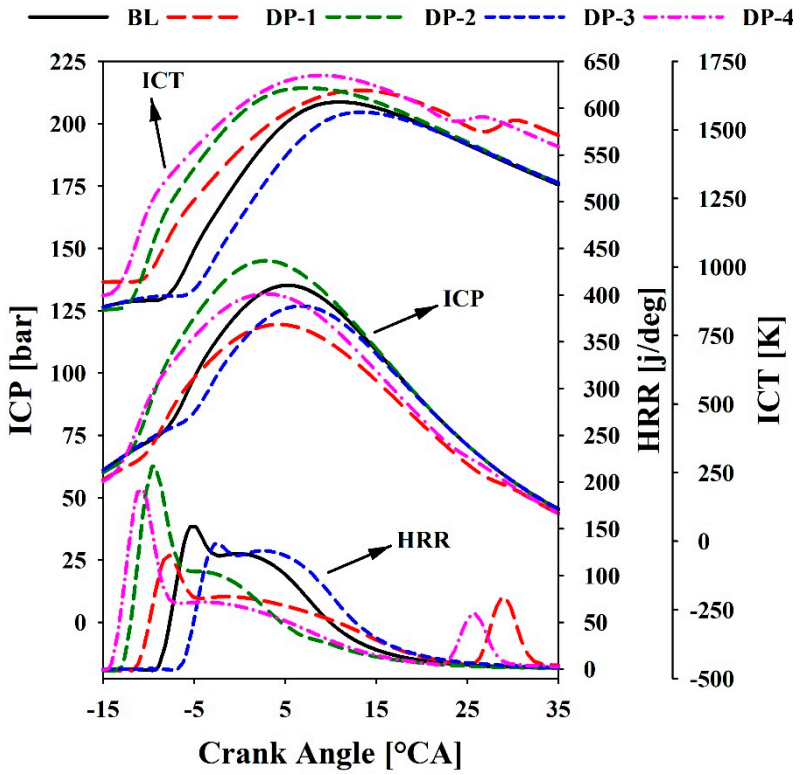

Figure 18. ICP, ICT and HRR patterns for the selected optimum design points.

Peak of HRR and, accordingly, maximum ICT and maximum ICP increased by advancing SoI (−20.7 °CA) at DP-2, which represents the "Low *bs*Soot" condition. Because of the increased ICT and introducing 2.6% post injection at α_{post}: 16.24 °CA, soot oxidation enhanced, and soot emission decreased by 81.97% to 0.0099 g/kWh. Due to quite low RGF (2.2292%) for α_{2IVO}: 155.11 °CA and high ICT, NO emission increased by 29.03% to 11.3523 g/kWh and BSFC increased by 2.97% to 199.4705 g/kWh due to deterioration in thermal efficiency caused by the growth in the portion of the pressure rise in the compression stroke due to advanced start of main injection.

At DP-3 which represents the "Low BSFC" condition, peak of HRR, maximum ICP and maximum ICT decreased with respect to the baseline case by delaying SoI (−11.99 °CA aTDC) and almost without applying iEGR (RGF: 1.3725%) and post injection (PFQ: 0.65%). The portion of the ICP rise in the compression stroke decreased and the angle at which the ICP is maximum shifted towards the expansion stroke. Thus, BSFC decreased by 0.68% from 193.7229 to 192.4023 g/kWh due to increased thermal efficiency. On the other hand, with the delay of SoI, due to the lower ICT, soot emission increased by 75.77% from 0.0549 to 0.0965 g/kWh, while NO emission decreased by 17.62% from 8.7983 to 7.2478 g/kWh.

At DP-4, which states the "low *bs*NO & *bs*Soot" condition, soot formation reduced by advancing SoI to −22.92 °CA aTDC, while NO formation was diminished by re-opening the intake valve at α_{2IVO}: 188.66 °CA (RGF: 20.9297%). As the advanced SoI dominated the RGF rise in terms of ignition delay, the peak of HRR increased with respect to the baseline case and maximum ICT rose due to combined effect of increased peak of HRR and iEGR. The main injection quantity reduced due to the post injection and majority of the heat was released in the compression stroke further away from the TDC caused by the advanced SoI. Therefore, the maximum ICP decreased and shifted towards TDC as compared to the baseline condition and BSFC increased by 7.6% to 208.4541 g/kWh due to worsened thermal efficiency. By introducing 10.47% post injection for α_{post}: 33.84 °CA in addition to advancing the SoI and applying iEGR, bsNO and *bs*Soot decreased by 32.16% and 30.6% to 5.9689 and 0.0381 g/kWh respectively.

4. Conclusions

The following conclusions can be drawn within the limitations of this study, which includes numerical analysis of post-injection and iEGR applications and multi-objective pareto optimization performed for a diesel engine running at 1500 rpm speed and 8.47 bar BMEP load condition.

1. With the application of 2IVO, up to 28.81% RGF can be provided for the specified operating conditions in the range of α_{2IVO}: 149 °CA–210 °CA for h_{2IVO}: 3 mm.
2. The iEGR increases the ICT, but NO emission is significantly reduced by diluting the in-cylinder charge. In contrast, soot and BSFC deteriorate due to the decrease in oxygen concentration and volumetric efficiency.
3. Post injection has significant potential to reduce soot emission in cases where it is not very close to the main injection, and optimal α_{post} in terms of soot emission delays as iEGR increases and SoI advances.
4. The increase in PFQ reduces NO emission. The soot formation rises with increasing PFQ in close post injection while it provides a greater reduction in soot emission at α_{post} angles where the soot emission is minimum.
5. The BSFC deteriorates by advancing the SoI from −15 °CA to −30 °CA as well as by delaying it to 0 °CA, and the positive effect of post injection on BSFC occurs only in early SoI timings, since it reduces the amount of fuel burned in the compression stroke.
6. The optimization results were found to be compatible with the study conducted to examine the effects of the iEGR and injection parameters on emissions and performance of the engine and show that simultaneous reduction of *bs*NO, *bs*Soot and BSFC relative to baseline is not possible for the operating conditions under consideration. On the other hand, thanks to the combined use of iEGR and post injection and proper adjustment of SoI; *bs*NO and *bs*Soot could be reduced simultaneously by 32.16% and 30.6%, respectively with only 7.6% increase in BSFC.

Author Contributions: Investigation, data curation, validation, software, formal analysis, writing—original draft, visualization, V.A.; supervision, methodology, investigation, writing—review and editing, O.Ö.; resources, software, investigation, C.B.; conceptualization, methodology, supervision, writing—review and editing, project administration, M.Ö. All authors have read and agreed to the published version of the manuscript.

Funding: This research was supported by the Republic of Turkey, Minister of Industry and Technology (0665.STZ.2014) with the partnership of TÜMOSAN Engine and Tractor Co.

Data Availability Statement: The data presented in this study are not publicly available due to privacy procedures of some of the participants of the study.

Acknowledgments: The authors would like to thank the TÜMOSAN Engine and Tractor Co. for their technical support and providing the GT-Power license.

Conflicts of Interest: The authors declare no conflict of interest.

Abbreviations

T_{in}	Intake air temperature [K]
P_{in}	Intake air pressure [bar]
P_{rail}	Rail pressure [bar]
m_{total}	Total injected fuel mass [mg]
m	Mass of the volume considered [kg]
$\dot{m}$	Boundary mass flux into volume [kg/s^{-1}]
u	Velocity at the boundary [m s^{-1}]
e	Total specific internal energy [kj kg^{-1}]
H	Total specific enthalpy [kj kg^{-1}]

h	Convective heat transfer coeff. [kW m^{-2} K^{-1}]
T_{fluid}	Gas temperature [K]
T_{wall}	Wall temperature [K]
P	Pressure [kPa]
ρ	Density [kg m^{-3}]
A	Cross-sectional flow area [m^2]
A_s	Heat transfer surface area [m^2]
V	Volume [m^3]
D	Equivalent diameter [m]
dx	Discretization length t [m]
dp	Pressure differential acting across dx [kPa]
C_f	Fanning friction factor [-]
K_p	Pressure loss coefficient [-]

References

1. Yeom, J.K.; Jung, S.H.; Yoon, J.H. An experimental study on the application of oxygenated fuel to diesel engines. *Fuel* **2019**, *248*, 262–277. [CrossRef]
2. Zhou, X.; Qian, W.; Pan, M.; Huang, R.; Xu, L.; Yin, J. Potential of n-butanol/diesel blends for CI engines under post injection strategy and di ff erent EGR rates conditions. *Energy Convers. Manag.* **2019**, 112329. [CrossRef]
3. O'Connor, J.; Musculus, M. Effects of exhaust gas recirculation and load on soot in a heavy-duty optical diesel engine with close-coupled post injections for high-efficiency combustion phasing. *Int. J. Engine Res.* **2014**, *15*, 421–443. [CrossRef]
4. Heywood, J.B. *Internal Combustion Engine Fundamentals*; McGraw-Hill: New York, NY, USA, 1988; ISBN 9780070286375.
5. Baratta, M.; Finesso, R.; Misul, D.; Spessa, E. Comparison between Internal and External EGR Performance on a Heavy Duty Diesel Engine by Means of a Refined 1D Fluid-Dynamic Engine Model. *SAE Int. J. Engines* **2015**, *8*. [CrossRef]
6. Maurya, R.K. *Characteristics and Control of Low Temperature Combustion Engines*; Springer International Publishing: Berlin/Heidelberg, Germany, 2018; ISBN 978-3-319-68507-6.
7. Gonzalez, M.A.D.; Di Nunno, D. Internal Exhaust Gas Recirculation for Efficiency and Emissions in a 4-Cylinder Diesel Engine. *SAE Tech. Pap.* **2016**. [CrossRef]
8. Balaji, J.; Ganesh Prasad, M.V.; Rao, L.N.; Bandaru, B.; Ramesh, A. Modelling and Experimental Study of Internal EGR System for NOx Control on an Off-Road Diesel Engine. *SAE Tech. Pap.* **2014**. [CrossRef]
9. Dronniou, N.; Lejeune, M.; Balloul, I.; Higelin, P. Combination of high EGR rates and multiple injection strategies to reduce pollutant emissions. *SAE Tech. Pap.* **2005**. [CrossRef]
10. Mohan, B.; Yang, W.; Chou, S.K. Fuel injection strategies for performance improvement and emissions reduction in compression ignition engines—A review. *Renew. Sustain. Energy Rev.* **2013**, *28*, 664–676. [CrossRef]
11. Hu, J.; Yao, C.; Geng, P.; Feng, J.; Liu, M.; Li, Z.; Wang, H. Effects of pilot injection strategy of diesel fuel on combustion characteristics in a premixed methanol-air mixture atmosphere in a CVCC. *Fuel* **2018**, *234*, 1132–1143. [CrossRef]
12. Jafarmadar, S. The Effect of Split Injection on the Combustion and Emissions in DI and IDI Diesel Engines. *Diesel Engine Combust. Emiss. Cond. Monit.* **2013**, 3–32. [CrossRef]
13. O'Connor, J.; Musculus, M.P.B. Effect of load on close-coupled post-injection efficacy for soot reduction in an optical, heavy-duty diesel research engine. *J. Eng. Gas Turbines Power* **2014**, 136. [CrossRef]
14. Yip, H.L.; Fattah, I.M.R.; Yuen, A.C.Y.; Yang, W.; Medwell, P.R.; Kook, S.; Yeoh, G.H.; Chan, Q.N. Flame–Wall Interaction Effects on Diesel Post-injection Combustion and Soot Formation Processes. *Energy Fuels* **2019**, *33*, 7759–7769. [CrossRef]
15. Zheng, M.; Asad, U.; Reader, G.T.; Tan, Y.; Wang, M. Energy efficiency improvement strategies for a diesel engine in low-temperature combustion. *Int. J. Energy Res.* **2009**, *33*, 8–28. [CrossRef]
16. Millo, F.; Mallamo, F.; Arnone, L.; Bonanni, M.; Franceschini, D. Analysis of different internal EGR solutions for small diesel engines. *SAE Tech. Pap.* **2007**, *2007*. [CrossRef]
17. Choi, H.; Lee, J.; Hong, K.; Lee, S.; Choi, S.; Yu, S.; Min, K. Comparison of the effects of multiple injection strategy on the emissions between moderate and heavy EGR rate conditions: Part 2-post injections †. *J. Mech. Sci. Technol.* **2013**, *27*, 2217–2223. [CrossRef]
18. Helmantel, A.; Golovitchev, V. Injection strategy optimization for a light duty di diesel engine in medium load conditions with high EGR rates. *SAE Tech. Pap.* **2009**. [CrossRef]
19. Hotta, Y.; Inayoshi, M.; Nakakita, K.; Fujiwara, K.; Sakata, I. Achieving lower exhaust emissions and better performance in an HSDI diesel engine with multiple injection. *SAE Tech. Pap.* **2005**, *2005*. [CrossRef]
20. Bobba, M.; Musculus, M.; Neel, W. Effect of post injections on in-cylinder and exhaust soot for low-temperature combustion in a heavy-duty diesel engine. *SAE Int. J. Engines* **2010**, *3*, 496–516. [CrossRef]
21. Almeida, F.L.; Zoldak, P.; Wang, Y.; Sobiesiak, A.; Lacava, P.T. Multi-dimensional engine modeling study of egr, fuel pressure, post-injection and compression ratio for a light duty diesel engine. In Proceedings of the ASME 2014 Internal Combustion Engine Division Fall Technical Conference, ICEF 2014, Web Portal ASME (American Society of Mechanical Engineers), Columbus, IN, USA, 19–22 October 2014; Volume 2.

22. Cho, I.; Lee, Y.; Lee, J. Investigation on the Effects of Internal EGR by Variable Exhaust Valve Actuation with Post Injection on Auto-ignited Combustion and Emission Performance. *Appl. Sci.* **2018**, *8*, 597. [CrossRef]
23. GT-SUITE Flow Theory Manual, Gamma Technologies, Westmont, Illinois, USA, 2017. Available online: http://www.gtisoft.com (accessed on 22 December 2020).
24. Rodrigues De Souza, G.; De Castro Pellegrini, C.; Ferreira, S.L.; Soto Pau, F.; Armas, O. Study of intake manifolds of an internal combustion engine: A new geometry based on experimental results and numerical simulations. *Therm. Sci. Eng. Prog.* **2019**. [CrossRef]
25. Rakopoulos, C.D.; Hountalas, D.T.; Taklis, G.N.; Tzanos, E.I. Analysis of combustion and pollutants formation in a direct injection diesel engine using a multi-zone model. *Int. J. Energy Res.* **1995**, *19*, 63–88. [CrossRef]
26. Andric, J.; Schimmel, D.; Sediako, A.D.; Sjoblom, J.; Faghani, E. Development and Calibration of One Dimensional Engine Model for Hardware-In-The-Loop Applications. *SAE Tech. Pap. Ser.* **2018**, *1*, 1–8. [CrossRef]
27. Lavole, G.A.; Heywood, J.B.; Keck, J.C. Experimental and Theoretical Study of Nitric Oxide Formation in Internal Combustion Engines. *Combust. Sci. Technol.* **1970**, *1*, 313–326. [CrossRef]
28. Nagle, J.; Strickland-Constable, R.F. Oxidation of Carbon Between 1000–2000 °C. *Proc. Fifth Conf. Carbon* **1962**, 154–164. [CrossRef]
29. Hohenberg, G.F. *Advanced Approaches for Heat Transfer Calculations*; SAE International: Warrendale, PA, USA, 1979.
30. Park, S.; Cho, J.; Park, J.; Song, S. Numerical study of the performance and NOx emission of a diesel-methanol dual-fuel engine using multi-objective Pareto optimization. *Energy* **2017**, *124*, 272–283. [CrossRef]
31. Deb, K.; Jain, H. An evolutionary many-objective optimization algorithm using reference-point-based nondominated sorting approach, Part I: Solving problems with box constraints. *IEEE Trans. Evol. Comput.* **2014**, *18*, 577–601. [CrossRef]
32. Cho, J.; Park, S.; Song, S. The effects of the air-fuel ratio on a stationary diesel engine under dual-fuel conditions and multi-objective optimization. *Energy* **2019**, *187*, 115884. [CrossRef]
33. Hiroyasu, T.; Miki, M.; Kamiura, J.; Watanabe, S.; Hiroyasu, H. Multi-objective optimization of diesel engine emissions and fuel economy using genetic algorithms and phenomenological model. *SAE Tech. Pap.* **2002**. [CrossRef]
34. Chen, Y.; Zhu, Z.; Chen, Y.; Huang, H.; Zhu, Z.; Lv, D.; Pan, M.; Guo, X. Study of injection pressure couple with EGR on combustion performance and emissions of natural gas-diesel dual-fuel engine. *Fuel* **2020**, *261*, 116409. [CrossRef]
35. Pedrozo, V.B.; May, I.; Lanzanova, T.D.M.; Zhao, H. Potential of internal EGR and throttled operation for low load extension of ethanol-diesel dual-fuel reactivity controlled compression ignition combustion on a heavy-duty engine. *Fuel* **2016**, *179*, 391–405. [CrossRef]
36. Zheng, Z.; Yao, M. Mechanism of oxygen concentration effects on combustion process and emissions of diesel engine. *Energy Fuels* **2009**, *23*, 5835–5845. [CrossRef]
37. Bao, Z.; Kishigami, R.; Horibe, N.; Kawanabe, H.; Ishiyama, T. The effect of close post injection on combustion characteristics and cooling loss reduction. *Fuel* **2020**, *268*, 117294. [CrossRef]
38. Park, Y.; Bae, C. Effects of single and double post injections on diesel PCCI combustion. *SAE Tech. Pap.* **2013**, *1*. [CrossRef]
39. Zheng, Z.; Yue, L.; Liu, H.; Zhu, Y.; Zhong, X.; Yao, M. Effect of two-stage injection on combustion and emissions under high EGR rate on a diesel engine by fueling blends of diesel/gasoline, diesel/n-butanol, diesel/gasoline/n-butanol and pure diesel. *Energy Convers. Manag.* **2015**, *90*, 1–11. [CrossRef]
40. Oguma, M.; Goto, S.; Konno, M.; Sugiyama, K.; Mori, M. *Experimental Study of Direct Injection Diesel Engine Fueled with Two Types of Gas To Liquid (GTL)*; SAE International: Warrendale, PA, USA, 2002; Volume 111.
41. Jia, H.; Yin, B.; Wang, J.; Chen, L. Visualizations of combustion and emissions characteristics in a light-duty diesel engine with achieved premixed low temperature combustion. *Int. J. Automot. Technol.* **2015**, *16*, 201–209. [CrossRef]
42. Teoh, Y.H.; Masjuki, H.H.; Kalam, M.A.; How, H.G. Effect of injection timing and EGR on engine-out-responses of a common-rail diesel engine fueled with neat biodiesel. *RSC Adv.* **2015**, *5*, 96080–96096. [CrossRef]
43. Wei, M.; Li, S.; Liu, J.; Guo, G.; Sun, Z.; Xiao, H. Effects of injection timing on combustion and emissions in a diesel engine fueled with 2,5-dimethylfuran-diesel blends. *Fuel* **2017**, *192*, 208–217. [CrossRef]
44. Teoh, Y.H.; Masjuki, H.H.; How, H.G.; Kalam, M.A.; Yu, K.H.; Alabdulkarem, A. Effect of two-stage injection dwell angle on engine combustion and performance characteristics of a common-rail diesel engine fueled with coconut oil methyl esters-diesel fuel blends. *Fuel* **2018**, *234*, 227–237. [CrossRef]
45. Liu, W.; Song, C. Effect of post injection strategy on regulated exhaust emissions and particulate matter in a HSDI diesel engine. *Fuel* **2016**, *185*, 1–9. [CrossRef]
46. Gunabalan, A.; Tamilporai, P.; Ramaprabhu, R. Effects of Injection Timing and EGR on DI Diesel Engine Performance and Emission-using CFD. *J. Applied Sci.* **2010**, *9*. [CrossRef]
47. Fischer, S.; Stein, J.O. Investigation on the effect of very high fuel injection pressure on soot-NOx emissions at high load in a passenger car diesel engine. *SAE Tech. Pap.* **2009**, *2*, 1737–1748. [CrossRef]
48. Luo, J.; Liu, H.F. Study on the Mechanism of Soot Reduction by Multi-Injection Coupled with EGR. *Adv. Mater. Res.* **2013**, *805–806*, 1759–1762. [CrossRef]
49. Payri, F.; Benajes, J.; Pastor, J.V.; Molina, S. Influence of the post-injection pattern on performance, soot and NOx emissions in a HD diesel engine. *SAE Tech. Pap.* **2002**, *2002*. [CrossRef]
50. Liu, J.; Ma, B.; Zhao, H. Combustion parameters optimization of a diesel/natural gas dual fuel engine using genetic algorithm. *Fuel* **2020**, *260*, 116365. [CrossRef]
51. Kokjohn, S.L.; Reitz, R.D. A computational investigation of two-stage combustion in a light-duty engine. *SAE Int. J. Engines* **2009**, *1*, 1083–1104. [CrossRef]